RSC Advances

PAPER

View Article Online
View Journal | View Issue

Cite this: *RSC Adv.*, 2019, **9**, 6346

Construction of ultrathin MnO_2 decorated graphene/carbon nanotube nanocomposites as efficient sulfur hosts for high-performance lithium–sulfur batteries†

Nan Wang, Sikan Peng, Xiang Chen, Jixian Wang, Chen Wang, Xin Qi, Shenglong Dai and Shaojiu Yan*

Received 12th January 2019
Accepted 15th February 2019

DOI: 10.1039/c9ra00292h

rsc.li/rsc-advances

Lithium–sulfur batteries are attracting significant attention due to their high theoretical specific capacity and low cost. However, their applications are hindered by the poor conductivity of sulfur and capacity fading caused by the shuttle effect. Here, ultrathin manganese dioxide decorated graphene/carbon nanotube nanocomposites are designed as sulfur hosts to suppress the shuttle effect and improve the adsorption efficiency of polysulfides. The graphene/carbon nanotube hybrids, with extraordinary conductivity and large surface area, function as excellent channels for electron transfer and lithium ion diffusion. The ultrathin manganese dioxide nanosheets enable efficient chemical interaction with polysulfides and promote the redox kinetics of polysulfides. As a result, an ultrathin manganese dioxide decorated graphene/carbon nanotube sulfur composite with high sulfur content (81.8 wt%) delivers a high initial specific capacity of 1015.1 mA h g^{-1} at a current density of 0.1C, high coulombic efficiency approaching 100% and high capacity retention of 84.1% after 100 cycles. The nanocomposites developed in this work have promising applications in high-performance lithium–sulfur batteries.

1. Introduction

The lithium–sulfur (Li–S) battery is a promising candidate for next-generation commercial rechargeable batteries because of its high theoretical specific capacity (1675 mA h g^{-1}) and superior specific energy (2600 W h kg^{-1}).[1–3] It has great potential applications in electric vehicles and renewable energy storage. Moreover, sulfur, one of the most abundant elements on Earth, is environmentally friendly and inexpensive. However, the commercialization of the Li–S battery is hindered by two major challenges: (1) S and its discharge products (Li_2S_2/Li_2S) are intrinsically non-conducting, which lowers the S utilization and limits the battery rate performance; (2) the dissolution of lithium polysulfide species (LiPSs) in the electrolyte results in the shuttle effect and uncontrolled deposition of Li_2S_2 and Li_2S, which is responsible for low coulombic efficiency and severe capacity fading of the battery.[4,5] In an attempt to tackle these issues, various carbon materials such as activated carbon,[6] mesoporous carbon,[7] hollow carbon sphere,[8] carbon nanotubes (CNTs)[9,10] and graphene[11] have been employed as sulfur host and conductive framework to suppress shuttle effect and enhance redox kinetics of LiPSs. The carbon materials can accelerate the electron transfer, however, the intrinsically nonpolar carbon hosts exhibit rather weak physisorption toward LiPSs, which cannot efficiently suppress the polysulfides shuttle effect and accomplish the controlled deposition of Li_2S_2 and Li_2S.[12,13] Although $LiNO_3$ was added in the electrolyte to protect anode by forming solid electrolyte interphase (SEI) layer, its result is still limited in long-term cycle. Therefore, materials with strong chemical adsorption toward LiPSs are expected to achieve stable cycle performance for the Li–S batteries.

Recently, metal oxides such as TiO_2,[1] MnO_2,[14] Mn_3O_4,[15] Co_3O_4,[16] VO_2,[17] and V_2O_5 [18] have been found to effectively mitigate LiPSs shuttling *via* strong chemical interaction with the LiPSs, because of their inherently hydrophilic surfaces.[19] The cycling performance of Li–S batteries has been significantly improved by chemical adsorption of metal oxides in immobilizing LiPSs.[20] Nevertheless, the poor conductivity of metal oxides inevitably lowers the LiPSs redox reactions and compromises the rate capability of Li–S batteries.[21,22] Recently, the performance of Li–S batteries has been improved by coupling polar metal oxides with conductive carbon materials, which enhance the conductivity of carbon–metal oxide composite as sulfur host. As an effective trapper for LiPSs, MnO_2 has been widely applied in Li–S batteries because of its earth abundance, low-cost and environmental friendliness. Nazar and co-workers recently reported that MnO_2 exhibited strong chemical trapping of LiPSs, with thiosulfate ($S_2O_3^{2-}$) serving as a surface-bound intermediate arising

---

Beijing Institute of Aeronautical Materials (BIAM), Beijing, 100095, P. R. China. E-mail: shaojiuyan@126.com

† Electronic supplementary information (ESI) available. See DOI: 10.1039/c9ra00292h

from the LiPSs reacting on the MnO_2 surface and promoted the controlled deposition of Li_2S_2/Li_2S.[14] Subsequently, they proved that MnO_2 with a redox potential E of 3.05 V lies in the target window ($2.4\ V < E \leq 3.05\ V$) directly correlated to the chemical interaction of polysulfides.[17] Liu and co-workers proved the enhanced electrochemical kinetics by using carbon nanofibers supported MnO_2 composite.[23] Ultrathin MnO_2 was employed in Li–S batteries and achieved a high capacity retention of 76.1% at 0.2C after 100 cycles.[24] Furthermore, large surface area, and uniform distribution of MnO_2 were also confirmed to enhance the adsorption ability towards LiPSs and facilitate the lithium ion diffusion.[21,24,25]

These results inspired us to design and construct a hybrid structure with ultrathin MnO_2 nanosheets uniformly distributed on the highly conductive carbon materials. Graphene/carbon nanotube (G/CNT) hybrids with CNTs covalently anchored on the graphene sheets, which have been proven to possess large surface areas, high porosity and outstanding conductivity,[26,27] are selected as conductive framework. In particular, G/CNT hybrids have been applied for Li–S batteries, which exhibit a high rate performance.[28] Until now, significant improvements on long-term cycling performance have been obtained by introducing MnO_2 as the trapper of LiPSs, however, a rapid capacity fading in the initial several cycles caused by insufficient adsorption are still worth of further investigation. In addition, high addition of MnO_2 will lower the energy density of the whole battery which is unsuitable for application of Li–S batteries. In this respect, more attentions should be paid to improving the adsorption efficiency which are identified by the strong interaction with sufficient adsorption sites as well as the fast conversion of LiPSs.

In this study, we report ultrathin MnO_2 nanosheets decorated G/CNT nanocomposites with efficient immobilization and improved redox kinetics of LiPSs as sulfur host for Li–S batteries. Several advantages can be expected for Li–S batteries. Firstly, G/CNT hybrids are selected as the framework because of their large specific surface area and porous structures, which should be beneficial for uniform distribution of MnO_2 nanosheets and high sulfur loading. Secondly, the composites demonstrate extraordinary electrical conductivity due to the unique three-dimensional (3D) conductive network, which should significantly enhance the charge transfer and facilitate the conversion of LiPSs. Finally, ultrathin MnO_2 nanosheets distributed uniformly on the surface of the carbon framework serve as anchoring points for LiPSs. That is, the ultrathin MnO_2 nanosheets with large surface areas maximize the chemical interaction between MnO_2 and LiPSs, which is expected to remarkably suppress shuttling effect and improve the adsorption efficiency. The G/CNT@MnO_2 composites as sulfur host prepared by this facile method is expected to demonstrate a promising performance of Li–S batteries.

1.1. Synthesis of G/CNT@MnO_2 and pure MnO_2

G/CNT obtained from Beijing Beifang Guoneng New Material Co., Ltd., were used as received, and the typical preparing procedures can be referenced to the method as reported previously.[28] First, 100 mg G/CNT was dispersed in 500 ml of distilled water. This was followed by a 10 min ultrasonic treatment to form a stable dispersion solution, which was then transferred for magnetic stirring. Excessive ethanol was added dropwise under vigorous stirring. Finally, 27 mg of $KMnO_4$ was added to the above dispersion solution. The reaction was performed at ambient temperature for 12 h. The obtained precipitate was filtered with vacuum and washed, first with distilled water and then ethanol. Finally, the purified precipitation was desiccated at 80 °C for 12 h in a thermoelectric thermostat drying oven. Hence, a dark powder was obtained. Pure MnO_2 was synthesized through the same method without adding G/CNT hybrids.

1.2. Synthesis of G/CNT@S, G/CNT@MnO_2@S composites

The carbon–S composites were prepared *via* a typical melt diffusion strategy. The as-prepared samples (G/CNT, G/CNT@MnO_2) were first grinded with pure sulfur powder with a C/S mass ratio of 1 : 5. Subsequently, the mixture was transferred into a stainless-steel autoclave and sealed in a glovebox. Then, the autoclave was maintained at 155 °C for 24 h.

1.3. Preparation of Li_2S_6 additive electrolyte

The experiment was conducted in a glove box filled with argon (Ar). First, a 0.04 mol L^{-1} Li_2S_6 solution was prepared by adding 92 mg (2 mol) of Li_2S and 320 mg (10 mol) sublimed sulfur to 50 ml dimethoxyethane (DME) solution with vigorous stirring. Then, 1 ml of 0.04 mol L^{-1} Li_2S_6 solution was diluted into 0.004 mol L^{-1} using 9 ml of DME. Next, 40 mg G/CNT and G/CNT@MnO_2 composites were added to different samples of diluted Li_2S_6 solution, followed by stirring for 2 h. The supernatant was used for test in each case.

1.4. Characterization

The morphologies of the as-made samples were characterized using field emission scanning electron microscopy (FESEM; FEI NOVA NanoSEM 450). Further, transmission electron microscopy (TEM) and selected area electron diffraction (SAED) observations were executed utilizing a transmission electron microscope (FEI Tecnai G2 F30) at an accelerating voltage of 100 kV, which was equipped with a high-resolution accessory. Powder X-ray diffraction (XRD) patterns were obtained using a diffractometer (Bruker D8 advance) with copper K radiation (30 kV, 30 mA, $\lambda = 1.5406$ Å). In addition, Raman scattering spectra were taken at room temperature using a LabRAM HR800 Raman spectrometer (HORIBA, Japan). The thermal decomposition was investigated with a differential scanning calorimeter (DSC, NETZSCH) using an aluminum (Al) crucible. The specific surface area and pore size distribution were calculated based on the nitrogen (N) physical adsorption with a Kubo-X1000. XPS measurement was performed on a Thermo ESCALAB 250Xi with a monochromatic Al Kα source. Ultraviolet/visible (UV/vis) spectra were obtained using a Perkin-Elmer Lambda 950 spectrometer.

1.5. Preparation of electrodes and coin cells

The working electrode films were prepared by casting a uniform slurry of the active material (G/CNT@S, G/CNT@MnO_2@S), polyvinylidene difluoride, and HS-100 acetylene black (Denka, Japan) at a weight ratio of 80 : 10 : 10 in an *N*-methyl-2-pyrrolidinone solvent onto carbon-coated Al foil *via* the doctor blade casting method. The electrode film was dried thoroughly at 60 °C for 24 h in a vacuum oven and cut into round disks with 14 mm diameter. Then, 2016-type button cells were assembled, with Li foil as the anode, Celgard® 2325 membrane as the separator, and 1.0 mol L^{-1} Li bis(trifluoromethanesulfonyl)imide (LiTFSI) in DME/1,3-dioxolane (DOL) (1 : 1 v/v, with 1.0 wt% $LiNO_3$) as the electrolyte with electrolyte/sulfur ratio of 12 μl mg^{-1}. The final sulfur loading in the cathode is calculated to be about 65.4%. The areal sulfur loading was kept between 1.5 and 2.0 mg cm^{-2}.

1.6. Electrochemistry

The cycling performance and rate tests were performed using a LAND battery program-control test system (CT2001 A, Wuhan LAND Electronic Co., Ltd., China) within the voltage range of 1.7–2.8 V. The specific capacity values were calculated according to the mass of sulfur in the cathode. Cyclic voltammetry (CV) measurements were conducted using a CHI1000C instrument (Chenhua, China) between 1.7 and 2.8 V *vs.* Li^+/Li at a scanning rate of 0.1, 0.2, 0.3, 0.4, 0.6, 0.8 mV s^{-1}. Electrochemical impedance spectroscopy (EIS) measurements were performed using an electrochemical workstation (Zahner-Zennium, Germany) under the open circuit voltage over a frequency range of 100 kHz to 100 mHz. The amplitude of the alternating-current (AC) voltage was 5 mV.

2. Results and discussion

The synthesis process of the G/CNT@MnO_2@S composites is illustrated in Fig. 1. For comparison, G/CNT@S composites without MnO_2 decorating were also synthesized, as mentioned above. Firstly, the G/CNT hybrids fabricated *via* CVD method were selected as hosts for MnO_2 and sulfur.[28] Subsequently, ultrathin MnO_2 nanosheets were anchored *in situ* on the surface of G/CNT hybrids through redox deposition to ensure their uniform distribution. The proposed redox reactions are as follows:[29–31]

$$4MnO_4^- + 2OH^- + 3C \rightarrow 3CO_3^{2-} + H_2O + 4MnO_2\downarrow \quad (1)$$

$$4MnO_4^- + H^+ + 3CH_3CH_2OH \rightarrow 3CH_3COO^- + 5H_2O + 4MnO_2\downarrow \quad (2)$$

Note that carbon acts as the reducing agent and the substrate for the heterogeneous nucleation of MnO_2. Further, the excessive ethanol protects the carbon material from over-oxidation and reduces potassium permanganate to form MnO_2. Finally, sulfur nanoparticles were coated uniformly on the surface of the G/CNT@MnO_2 composites using the melt diffusion method.[28]

Fig. 2 shows SEM and TEM images of typical G/CNT hybrids and G/CNT@MnO_2 composites. The G/CNT hybrids, which have crumpled sheet-like porous structures, are composed of few-layer graphene and multiwalled CNTs (Fig. 2a–c). The CNTs covalently anchored on both sides of graphene flakes constructed a 3D architecture, which could inhibit the aggregation of both CNTs and graphene flakes and possess high surface area, porous structure and high conductivity (Fig. 2 and S1†). The G/CNT hybrids exhibit specific surface area of 1519.9 m^2 g^{-1}, with a large total pore volume of 2.56 cm^3 g^{-1}. The large specific surface area and sufficient porosity of the G/CNT hybrids indicate their feasibility for efficient sequestration and adsorption of highly loaded sulfur as well as uniform deposition of MnO_2 nanosheets.[32] Moreover, the crumpled sheet-like graphene and CNT construct a 3D conductive network which could provide large amount of charge transfer channels and Li^+ diffusion channels, thus suggesting high rate performance and rapid conversion of LiPSs.

In situ redox deposition was adopted to obtain ultrathin MnO_2 nanosheets and their uniform distribution. No obvious bulk MnO_2 were observed in the SEM image Fig. 2d indicates that MnO_2 nanosheets were uniformly anchored on the surface of G/CNT hybrids. Further, TEM was employed to explore the structure details of MnO_2. The ultrathin MnO_2 nanosheets with a lamellar structure and flexuous shape are observed in Fig. 2e, which are typical characteristics viewed along a direction parallel to the (001) plane.[33–35] The thickness of MnO_2 nanosheets is measured to be 4 nm on average, for which the stripe spacing of (001) plane is further measured to be 0.65 nm. In Fig. 2f, the lattice fringes having an interplanar spacing of 0.25 nm correspond to a δ-MnO_2 crystal which shows uniform distribution on the surface of G/CNT. The corresponding element mapping further confirms the uniform distribution of MnO_2 in the composites of G/CNT@MnO_2, which consistent with the results of SEM and TEM (Fig. S2†). The formation of ultrathin MnO_2 nanoflakes is likely due to the self-assembly of δ-MnO_2 nano-grains, which is controlled by a Coulomb interaction and driven by the demand for surface energy reduction.[33] It is reported that the Li_2S_x capture is dominated by monolayer chemisorption.[21] Therefore, ultrathin MnO_2 nanosheets with large surface area provide sufficient interfaces for chemical adsorption and reduce the addition of MnO_2, suggesting an enhancement of adsorption efficiency and improvement of specific energy of the batteries.

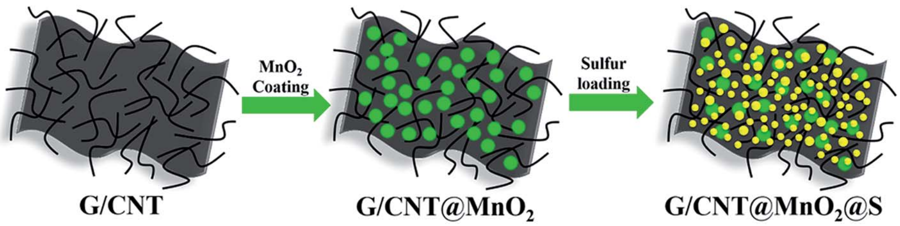

Fig. 1 Schematic illustration of G/CNT@MnO_2@S nanocomposite synthetic process.

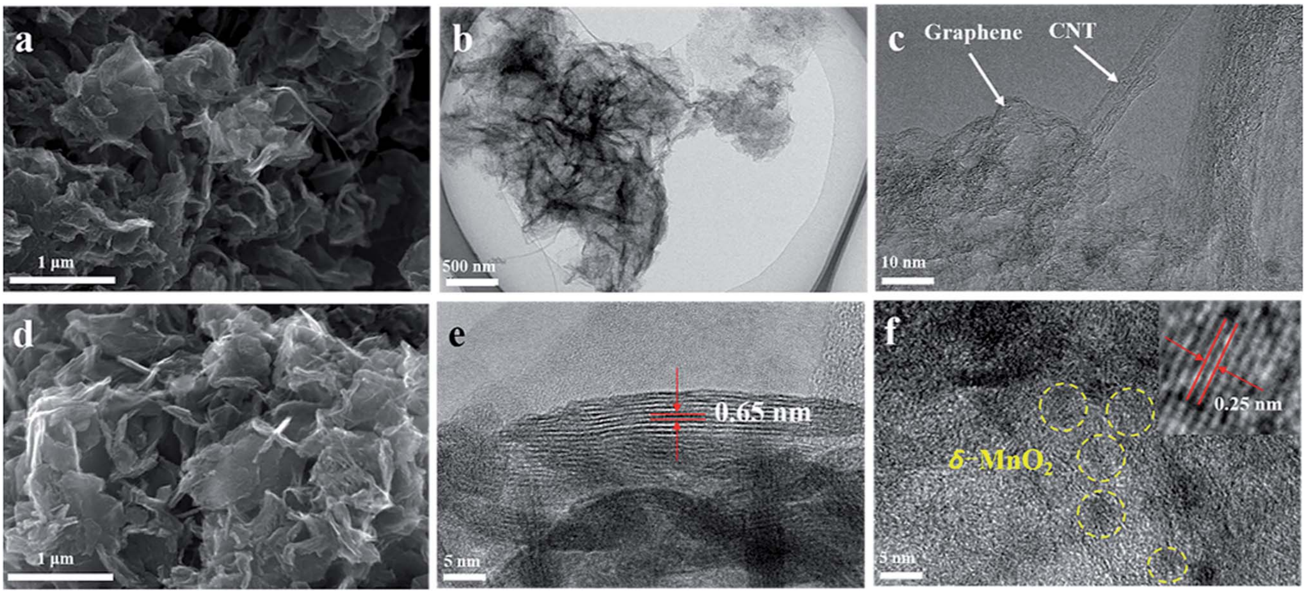

Fig. 2 (a) FESEM image of G/CNT. (b and c) TEM images of G/CNT. (d) FESEM image of G/CNT@MnO_2. (e and f) TEM images of G/CNT@MnO_2.

XRD measurements were conducted to determine the phase structure of the MnO_2 anchoring on the surface of G/CNT hybrids. Peaks centered at 12.5°, 25.2°, 37.3° and 65.6° were found, which match well with the (001), (002), ($\bar{1}$11) and (020) reflections of monoclinic birnessite, δ-MnO_2 (JCPDS no. 80-1098). This result reveals that the as-prepared δ-MnO_2 anchoring on the G/CNT is almost X-ray amorphous, indicating that δ-MnO_2 is composed of crystalline and amorphous parts, as reported previously (Fig. 3a).[29] It has also been reported that poorly crystalline form of manganese oxide will occur under low-temperature synthesis.[36]

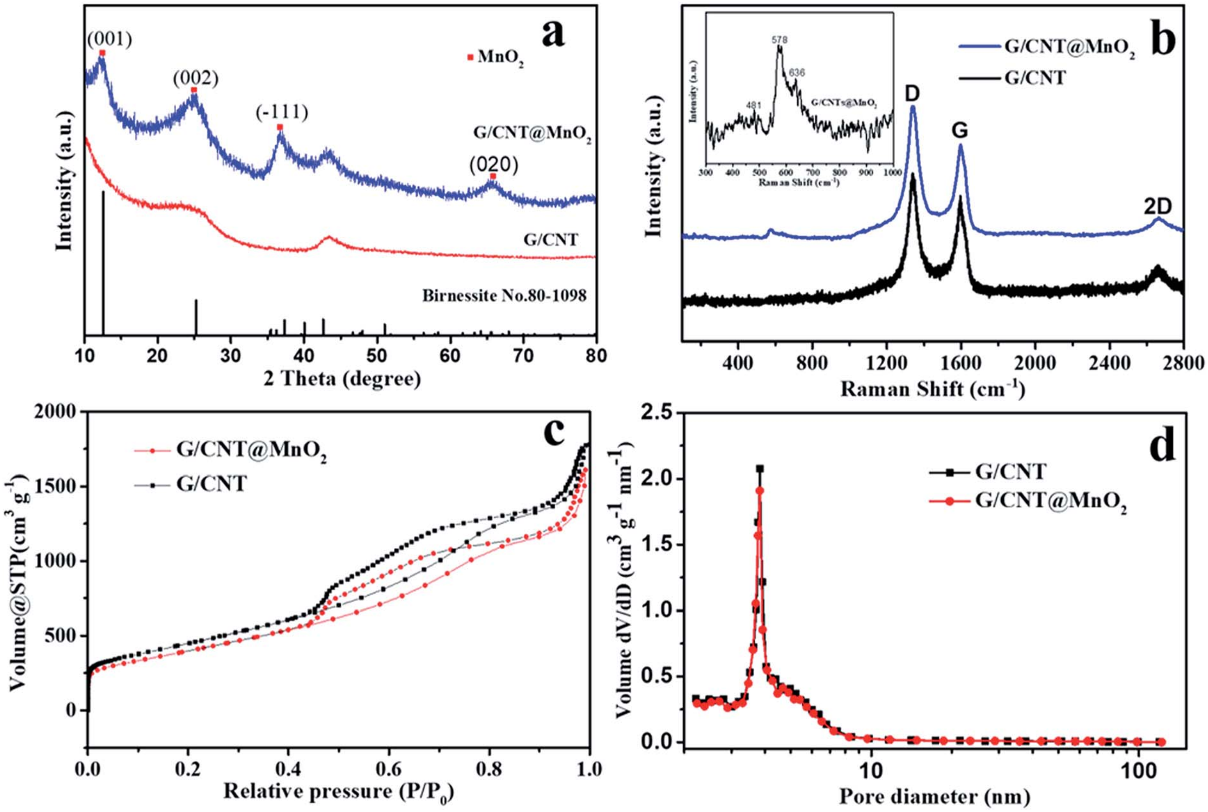

Fig. 3 (a) XRD patterns of G/CNT and G/CNT@MnO_2. (b) Raman spectra of G/CNT and G/CNT@MnO_2, inset image is magnification Raman shift of G/CNT@MnO_2. (c) N_2 adsorption/desorption isotherms for G/CNT and G/CNT@MnO_2. (d) BJH pore size distribution for G/CNT, G/CNT@MnO_2.

Raman technique is useful for analyzing the local structures of manganese dioxides, especially for samples with poor crystallinity.[37] Therefore, Raman technique was applied to analyze the as-prepared G/CNT@MnO_2 composites (Fig. 3b). Raman bands at 1346, 1597 and 2666 cm^{-1} are related to the D-band, G-band and 2D band of carbon materials in G/CNT hybrids. Furthermore, the G/CNT@MnO_2 composites demonstrate higher intensity ratio of D-band and G-band I_D/I_G (1.40) compared with G/CNT hybrids (1.19). This result indicates that the anchoring of MnO_2 on the surface of G/CNT caused more disordered carbon generated from the reaction of carbon and MnO_4^-.[38,39] As shown in the inset of Fig. 3b, three Raman bands located at 481, 578, and 636 cm^{-1} are in agreement with the three major vibration features of δ-MnO_2, which proves the presence of δ-MnO_2 and is in good accord with the result of XRD.[40] Further, the results of thermogravimetric analysis (TGA) demonstrate that the MnO_2 content in the G/CNT@MnO_2 composites is approximately 21 wt%, including 7 wt% water contained within the δ-MnO_2 (Fig. S3†). As reported in the literature, water molecules and cationic species are located between the sheets of MnO_6 octahedra to balance the charge.[41] The optimized MnO_2 content of 21 wt% in G/CNT@MnO_2 composites is in aim to balance the adsorption ability and the conductivity.

An N_2 adsorption analysis was performed to study the porosity of the G/CNT hybrids and G/CNT@MnO_2 composites (Fig. 3). A typical type-IV isotherm with a type-H3 hysteresis loop was obtained from the results of G/CNT and G/CNT@MnO_2 composites, indicating that the two composites are mainly composed of a mesoporous structure (Fig. 3c). The specific surface area of the G/CNT@MnO_2 was calculated to be 1431.8 $m^2\ g^{-1}$ *via* the Brunauer–Emmett–Teller (BET) method, being slightly lower than that of the G/CNT hybrids (1519.3 $m^2\ g^{-1}$). To evaluate the specific surface area of MnO_2 nanosheets on the surface of G/CNT, pure MnO_2 nanosheets were also revealed by BET method for reference which was calculated to be 114.3 $m^2\ g^{-1}$ (Fig. S4†). In addition, a typical type-III isotherm was obtained from the pure MnO_2 nanosheets indicating a nonporous structure which consists well with the results observed from the TEM images. Concluded from the BET results of G/CNT@MnO_2 composites and pure MnO_2, the MnO_2 nanosheets on the surface of G/CNT possess an ultrathin structure and large surface area which will provide sufficient adsorption sites, thus enhance the adsorption efficiency of LiPSs on the surface of MnO_2 nanosheets. The total pore volume of G/CNT@MnO_2 was calculated to be 2.49 $cm^3\ g^{-1}\ nm^{-1}$ and its Barrett–Joyner–Halenda (BJH) pore size distribution is shown in Fig. 3d. The result shows slightly pore volume decreasing after MnO_2 coating compared with that of G/CNT (2.56 $cm^3\ g^{-1}\ nm^{-1}$), but identical pore size distribution. The obtained results indicate that the G/CNT@MnO_2 composites still maintain a large surface area, pore volume and pore size distribution for high-content sulfur loading.

Next, sulfur was introduced into the G/CNT@MnO_2 composites by melt-diffusion method. The SEM and TEM images (Fig. 4a and b) show that sulfur particles were uniformly distributed, and no agglomerated sulfur particles were observed on the surfaces of the G/CNT@MnO_2@S composites which was further confirmed by the element mapping shown in Fig. S2.† Also, nanocrystal sulfur particles with an average diameter of 10 nm were observed in Fig. 4b. In addition, high-resolution TEM (HRTEM) imagery revealed that lattice fringes corresponding to interplanar spacings of 0.477 and 0.1789 nm is consistent with the (200) and ($\bar{1}\bar{7}1$) planes of orthorhombic sulfur, respectively (Fig. 4c). The presence of nano-size sulfur particles and their uniform distribution is favorable for improving the utilization of sulfur and reinforcing the cycling stability and rate performance of Li–S batteries.[42]

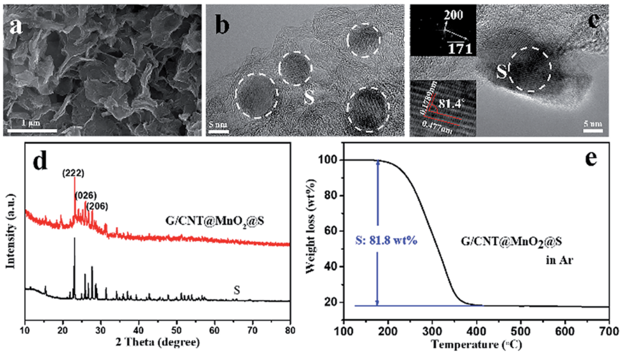

Fig. 4 (a) FESEM image. (b and c) TEM images. (d) XRD patterns and (e) TGA of G/CNT@MnO_2@S.

The XRD pattern of the G/CNT@MnO_2@S composites shows that the sulfur in the composites has the same orthorhombic structure as sulfur powder (Fig. 4d). Further, the Raman bands of the G/CNT@MnO_2@S composites are in good accordance with the three major bands of pure sulfur, also confirming the presence of sulfur in the composites (Fig. S5†). The surface chemical state of the G/CNT@MnO_2@S composites were further revealed by X-ray photoelectron spectroscopy (XPS). The survey spectrum confirms that the main elements of Mn, O, C, S coexist in the G/CNT@MnO_2@S composites (Fig. S6a†). In the C 1s spectrum (Fig. S6b†), the main peak at 284.8 eV is corresponding to sp^2 carbon (C–C or C=C) in graphene and carbon nanotubes. The peaks at 285.9 and 289.2 eV can be ascribed to carbon in C–O/C–S bounds and the carboxyl carbon (O–C=O) group, respectively.[43] The small amount of carbon species may be generated during carbon oxidation. As shown in Fig. S6c,† the peaks centered at 642.6 and 654.1 eV can be assigned to Mn $2p_{2/3}$ and Mn $2p_{1/2}$, which are both contributed by Mn^{4+} and reconfirm the existence of MnO_2.[43] In the S 2p spectrum (Fig. S6d†), the peaks located at 164.1 and 165.3 are corresponding to S–S group, whereas the peak at 169.1 eV can be attributed to the bond of sulfate species. The sulfate species may be generated from the redox interaction between S and MnO_2, which will facilitate the immobilization of LiPSs during cycling of Li–S batteries.[25] The sulfur loading of the G/CNT@MnO_2@S composites was determined to be approximately 81.8 wt% *via* TGA (Fig. 4e). And the sulfur content in the composite was further confirmed using elemental analysis (Table S1†). The high sulfur loading indicates a promising performance for practical application of Li–S batteries. After sulfur infiltration, the isotherm changed from type-IV to type-

III, and the specific surface area and pore volume of the G/CNT@MnO$_2$@S composites sharply decreased to 18.4 m^2 g^{-1} and 0.21 cm^3 g^{-1} nm^{-1} respectively, suggesting that S$_8$ molecules infiltrated the mesoporous parts of the G/CNT@MnO$_2$ composites (Fig. S7a and b†).

Next, the electrochemical performance of the G/CNT@MnO$_2$@S nanocomposites as cathode material for Li–S batteries was evaluated. To demonstrate the advantages of the MnO$_2$ anchoring effect, a similar G/CNT@S nanocomposites with sulfur loading of approximately 81.4 wt% was also synthesized and evaluated as a comparison. The CV profiles of the G/CNT@MnO$_2$@S cathode at 0.1 mV S^{-1} scan rate in the potential range of 1.7–2.8 V *vs.* Li/Li$^+$ for the first four cycles are shown in Fig. 5a. Two typical reduction peaks at 2.31 and 2.04 V were observed, because of the multiple reduction of sulfur. The peak at 2.31 V is related to the reduction of elemental S (S$_8$) to high-order polysulfides (Li$_2$S$_x$, $x \geq 4$), while the peak at 2.04 V is attributed to the further reduction of high-order polysulfides to low-order polysulfides (Li$_2$S$_x$, $1 < x < 4$) and Li$_2$S.[44] The oxidation peaks at 2.38 V correspond to the reverse oxidation of polysulfide (Li$_2$S/Li$_2$S$_2$) to the neutral S$_8$. In the four cycles, both the CV peak positions and area remained almost identical, suggesting good capacity stability and high reversibility of the G/CNT@MnO$_2$@S cathode.

The rate capability of the G/CNT@MnO$_2$@S cathode was evaluated by cycling at various current rates from 0.1 to 2C every 10 cycles, followed by recovery to 0.2C and 0.1C (Fig. 5b). This electrode delivered capacities of 1240.6, 897.5, 737.3, 638.1, and 538.3 mA h g^{-1} at 0.1C, 0.2C, 0.5C, 1C, 2C rates, respectively. Notably, after the C-rate is lowered back to 0.2C and 0.1C, the cathode can recover to 879.0 and 1045.7 mA h g^{-1} with stabilized capacity, which indicates the excellent electronic/ionic transport properties and reaction kinetics. In contrast, the discharge capacity of G/CNT@S electrode decreases rapidly with

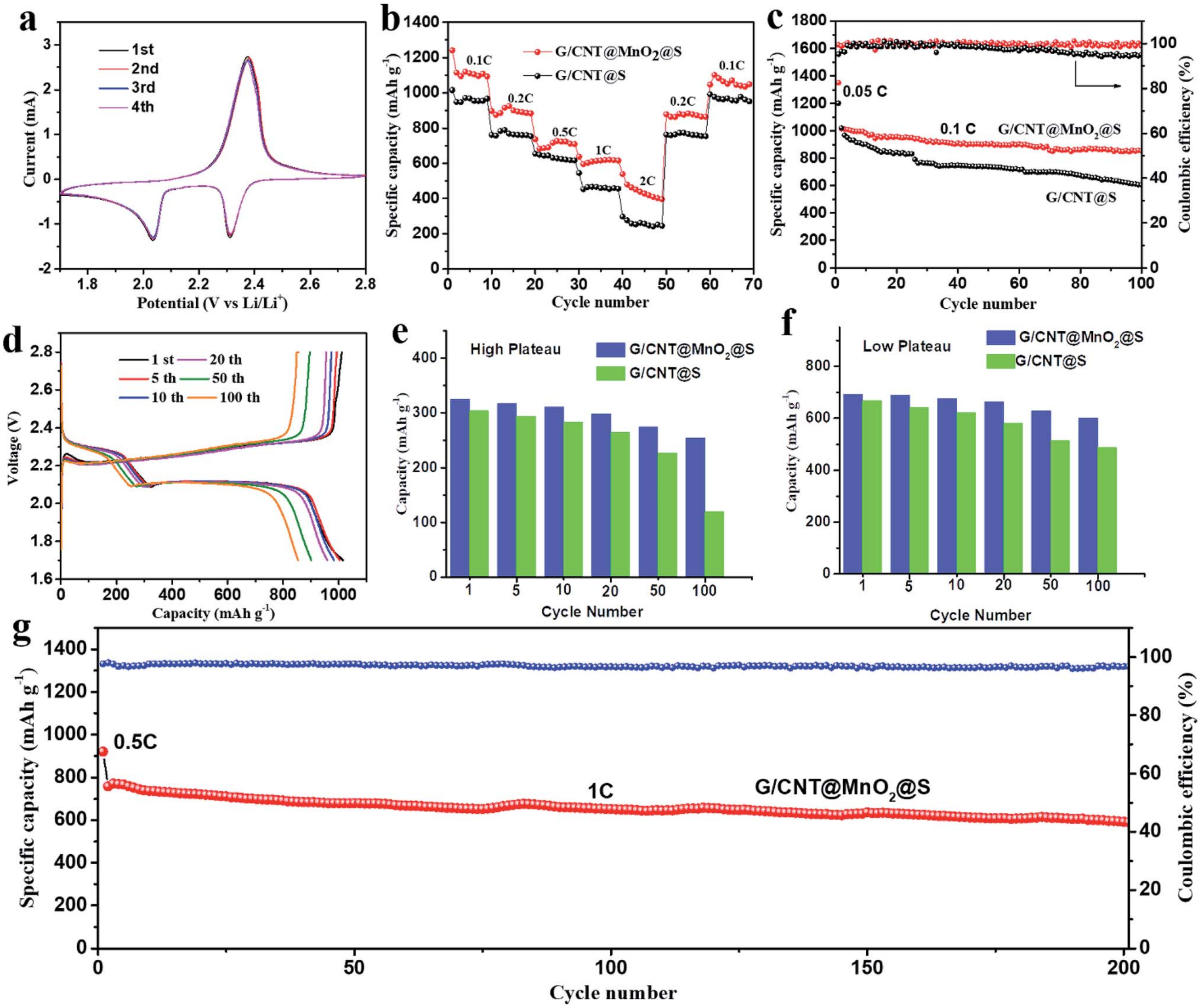

Fig. 5 (a) Cyclic voltammetry curves of G/CNT@MnO$_2$@S cathode swept in voltage range of 1.7–2.8 V *vs.* Li/Li$^+$ at a 0.1 mV s^{-1} sweep rate. (b) Rate performance of G/CNT@MnO$_2$@S cathode at C rates of 0.1–2C. (c) Cycle capacity and coulombic efficiency of G/CNT@MnO$_2$@S in comparison with G/CNT@S at 0.1C current density. (d) Voltage profiles of G/CNT@MnO$_2$@S at 0.1C. (e and f) High and low plateau discharge capacity for G/CNT@MnO$_2$@S and G/CNT@S. (g) Cycle capacity and coulombic efficiency of G/CNT@MnO$_2$@S cathode at 1C current density.

the increase of discharging rates. Furthermore, the galvanostatic charge–discharge voltage profiles of G/CNT@MnO_2@S electrode evaluated at various current rates (from 0.1C to 2C) are shown in Fig. S8a.† Two typical discharge plateaus at ≈2.33 and 2.08 V were observed in the discharge profile, corresponding to the production of high-order polysulfides and the subsequent deposition of low-order Li–S compounds, which agree well with the CV results described above. The galvanostatic charge–discharge voltage profiles of the G/CNT@S electrode are shown in Fig. S8b† (from 0.1C to 2C). Notably, the G/CNT@S cathode shows short discharge plateaus under a high rate of 2C compared to G/CNT@MnO_2@S cathode, indicating a higher polarization occurs.

Fig. 5c shows the cycling performance of the G/CNT@S and G/CNT@MnO_2@S cathodes at a current density of 0.1C (1C = 1675 mA h g^{-1}) in the voltage range of 1.7–2.8 V. The first cycle was charged and discharged at a current density of 0.05C and delivered a high capacity of 1349 mA h g^{-1}, which is 80.5% of theory capacity, indicating a high sulfur utilization. The G/CNT@MnO_2@S cathode delivered a high initial discharge capacity of 1015.1 mA h g^{-1} at a current density of 0.1C and remained at a capacity of 853.6 mA h g^{-1} after 100 cycles, corresponding to a high capacity retention of 84.1%. The coulombic efficiency was consistently near 100%, indicating that the shuttle effect was effectively restrained through the anchoring effect of the MnO_2 on the LiPSs. In contrast, the G/CNT@S electrode obtained a discharge capacity of 1021.4 mA h g^{-1} in the first cycle and suffered from a rapid decay after 100 cycles, with a remaining capacity of 605.1 mA h g^{-1} and a capacity retention of only 59.2%. The coulombic efficiency decreases rapidly after 50 cycles. Furthermore, the capacity retention of G/CNT@MnO_2@S cathode remains as high as 94% after 20 cycles and shows a smooth change compare with that of G/CNT@S cathode, which confirm a high adsorption efficiency of ultrathin MnO_2 nanosheets to LiPSs (Fig. S9†). The high capacity retention of G/CNT@MnO_2@S cathode could be ascribed to ultrathin MnO_2 nanosheets with large surface area which tender sufficient adsorption sites for LiPSs. Although $LiNO_3$ was added in the electrolyte to protect lithium anode from being consumed by forming SEI film, its role of suppressing shuttle effect is limited on long-term and high rate cycling due to the additive consumption.[45,46] However, the positive effect of $LiNO_3$ on improving safety of the batteries for application is worth considering.[47] The MnO_2 contribution to the capacity could be ignored, because of this material's low specific capacity and low ratio in the composites.[45,48]

The galvanostatic charge–discharge voltage profiles of G/CNT@MnO_2@S during cycles at 0.1C are shown in Fig. 5d. The discharging/charging plateaus are clearly discerned in the voltage-capacity results. The first three discharge curves (1st, 5th and 10th cycle) nearly overlapped with each other and the capacity only slightly faded in the first 20 cycles, which all suggest an enhanced reversibility of G/CNT@MnO_2@S cathode compared with G/CNT@S cathode (Fig. S10a†). This result is in good agreement with the observation in the CV profile. In addition, the discharging/charging plateaus of G/CNT@MnO_2@S cathode at the 20th cycle shows smaller polarization (0.17 V), longer voltage plateau and smaller overpotentials for nucleation of Li_2S_2 when compared with G/CNT@S cathode (Fig. S10b†), which exhibits accelerated electrodeposition kinetics from Li_2S_4 to Li_2S_2/Li_2S.[22,49] To evaluate superiority of the G/CNT@MnO_2 composite in the battery, discharge capacity of G/CNT@MnO_2@S and G/CNT@S cathodes were divided into high plateau and low plateau capacity separately as plotted in Fig. 5e and f. The high plateau capacity for G/CNT@MnO_2@S shows higher cycling stability compared with that of G/CNT@S, which confirms the effective suppression of LiPSs (Li_2S_x, $x \geq 4$) dissolution due to the high adsorption efficiency of ultrathin MnO_2 nanosheets. In the process of conversion from Li_2S_4 to Li_2S_2/Li_2S, the low plateau capacity for G/CNT@MnO_2@S is more stable than that of G/CNT@S, indicating the enhanced kinetics during the conversion of LiPSs to lithium sulfides. Therefore, the G/CNT@MnO_2 could not only immobilize the LiPSs through strong chemical interaction but also facilitate fast conversion of LiPSs and lithium sulfides.

The high rate cycling stability of the G/CNT@MnO_2@S cathode was further evaluated at a current density of 1C, as shown in Fig. 5g. The discharging and charging current density of the first cycle was 0.5C. Further, the initial discharging capacity of the G/CNT@MnO_2@S at a current density of 1C was 758.1 mA h g^{-1}, yielding a high capacity retention of 77.9% after 200 cycles with a high coulombic efficiency above 97%. The cycling performance of G/CNT@MnO_2@S cathode was compared with other related state-of-the-art cathodes based on carbon/MnO_2 host materials (Table S2†).[19,23,25,41,43,46,50–52] Apparently, the G/CNT@MnO_2@S cathode exhibits excellent cycling stability. Especially, the cathode exhibits a high capacity retention of 84.1% and 77.9% at a rate of 0.1C and 1C after cycling, respectively, which is comparable to or even better than almost all of previously reported results listed in Table S2.† Furthermore, some results shows good long-term cycling performance, however, the rapid capacity fading in the first several cycles has not yet been solved, which may be due to the low adsorption efficiency of MnO_2.

To evaluate the adsorption ability of the G/CNT@MnO_2 composites with regard to the LiPSs, the same amount of G/CNT and G/CNT@MnO_2 were added to the LiPSs solution. The LiPSs solution (mainly Li_2S_6) was prepared in accordance with the process described in previous reports and stirred for 2 h.[53,54] As shown in Fig. 6, the Li_2S_6 solution changed color from dark

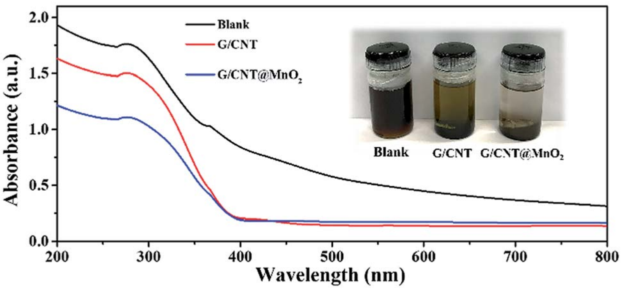

Fig. 6 UV-vis spectra of bare Li_2S_6 solution, G/CNT–Li_2S_6 solution, and G/CNT@MnO_2– Li_2S_6 solution, inset image is photograph of color changes after addition of G/CNTs and G/CNT@MnO_2 to Li_2S_6 solution with 2 h stirring.

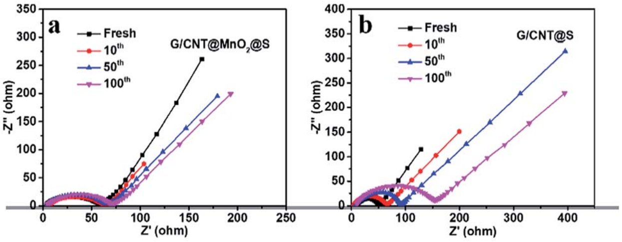

Fig. 7 Nyquist plots of (a) G/CNT@MnO$_2$@S electrode and (b) G/CNT@S electrode after different stages of discharge/charge cycling at the rate of 1C.

brown initially to yellow or colorless with the addition of the G/CNTs or G/CNT@MnO$_2$, respectively, suggesting the G/CNT@MnO$_2$ composites exhibit stronger adsorption ability for Li_2S_6 polysulfides compared with G/CNT. The adsorption ability of G/CNT@MnO$_2$ for LiPSs was further characterized through UV-vis spectroscopy. As shown in Fig. 6, the typical absorption peak at 278 nm of Li_2S_6 in the DME solution confirms that the solution was mainly composed of Li_2S_6.[55] Further, the adsorption peak intensity of the Li_2S_6 decreases with the addition of G/CNT and G/CNT@MnO$_2$, corresponding well to the color change of the Li_2S_6 solution. The observations are in good agreement with the results of cycling performance discussed above and thereby re-confirming the significant role of MnO$_2$ in trapping the LiPSs and their great contribution to the cycling stability.

To further evaluated the charge transfer and cycling stability of the cathodes, interfacial resistance at different cycles of G/CNT@MnO$_2$@S and G/CNT@S cathodes were investigated by electrochemical impedance spectroscopy (EIS). As shown in Fig. 7, all the results show a single semicircle in high frequency, and an oblique line in the low frequency, respectively, which are attributed to the charge transfer process (R_{ct}) and lithium ion diffusion in the cathode.[43] The two cathodes both exhibit a low resistance before cycling, of which G/CNT@MnO$_2$@S cathode yields a little higher resistance (Fig. 7). This is due to the poor conductivity of MnO$_2$, which slightly reduce the conductivity of G/CNT@MnO$_2$@S cathode. As shown in Fig. 7a, a stable and low resistance after 10, 50, and even the 100 cycles of G/CNT@MnO$_2$@S cathode indicates the strong anchoring effect and enhanced redox conversion of LiPSs. On the contrary, a remarkable resistance increasing after 10, 50, and 100 cycles occurred in G/CNT@S cathode, which could be due to the formation of uncontrolled precipitation of nonconductive Li_2S_2/Li_2S films on surface of G/CNT@S cathode (Fig. 7b).

CV measurements at various scanning rates were carried out to determine the lithium ion diffusion coefficient in the sulfur redox process. As shown in Fig. 8, all cathodic and anodic peak currents are linear with the square root of scan rates, indicating that the reactions are diffusion controlled.[23] The lithium ion diffusion coefficient can be calculated from classical Randles–Sevcik equation:

$$I_p = 2.69 \times 10^5 n^{1.5} A D^{0.5} C v^{0.5}$$

where I_p is the current peak, n stands for the number of electrons transferred in the reaction, A represents the active cathode area (1.54 cm^2), D is the diffusion coefficient, C is the concentration of lithium ion in electrolyte and v is the scan rate.[21] The parameters of n, A and C are constant in this battery system. The calculated lithium ion diffusion coefficients of G/CNT@MnO$_2$@S and G/CNT@S are shown in Fig. 8c–f and Table

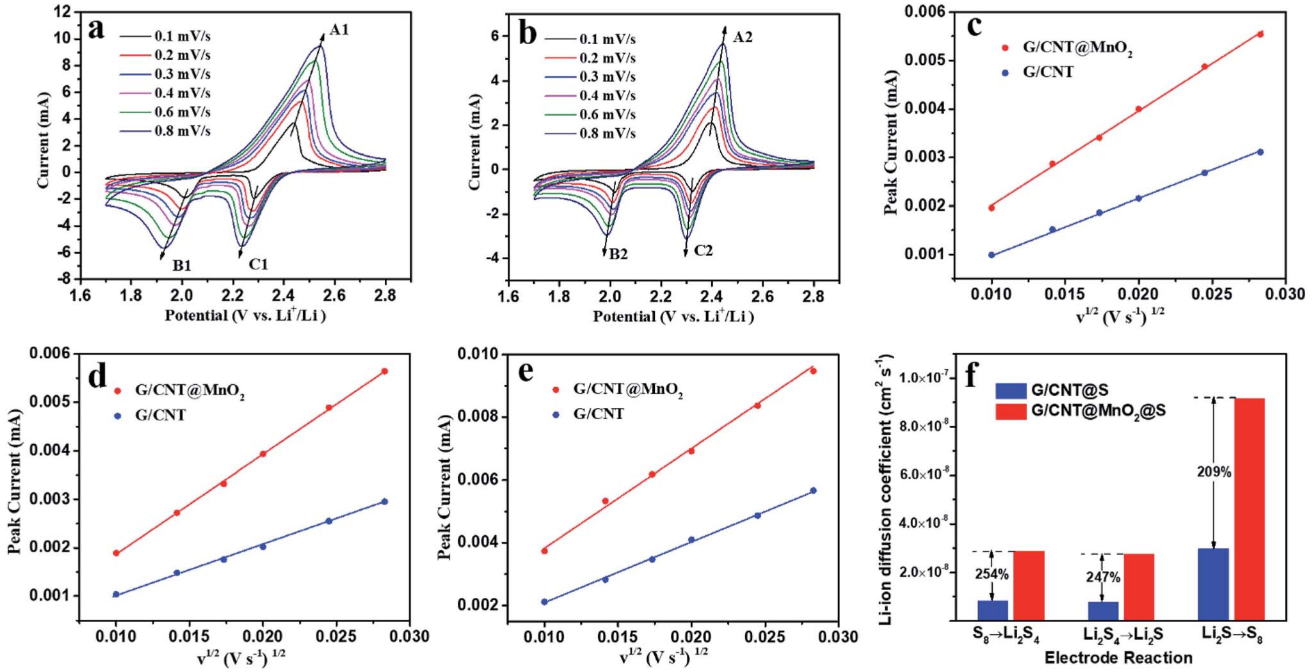

Fig. 8 (a and b) CV curves measured at various scan rates for G/CNT@MnO$_2$@S electrode and G/CNT@S electrode. (c–e) Relationship between peak currents and sweep rates of the cathodic reaction of $S_8 \rightarrow Li_2S_4$, the cathodic reaction of $Li_2S_4 \rightarrow Li_2S$ and the anodic reaction of $Li_2S \rightarrow S_8$. (f) Calculated diffusion coefficient of lithium ion.

Table 1 The list of the calculated diffusion coefficient of lithium ions

Diffusion coefficient ($cm^2 s^{-1}$)	Cathodic reaction, $S_8 \rightarrow Li_2S_4$	Cathodic reaction, $Li_2S_4 \rightarrow Li_2S$	Anodic reaction, $Li_2S \rightarrow S_8$
G/CNT@MnO_2@S	2.87×10^{-8}	2.74×10^{-8}	9.17×10^{-8}
G/CNT@S	8.28×10^{-9}	7.74×10^{-9}	2.965×10^{-8}

1. The lithium ion diffusion coefficients of G/CNT@MnO_2@S are much higher than those reported previously,[46,56] which can be attributed to existence of 3D architecture of G/CNT hybrids and ultrathin MnO_2 nanosheets, which provide amounts of Li ion diffusion channels. The lithium ion diffusion coefficients of G/CNT@MnO_2@S cathode at different redox process are twice higher than that of G/CNT@S cathode, suggesting the acceleration of lithium ion diffusion and enhancement of the reaction kinetics.[56] Besides, the slight positive shift in the reduction peak and negative shift in the oxidation peak of G/CNT@MnO_2@S cathode also derive from the poor conductivity of MnO_2 which is in accordance with the results of EIS.

With the above discussions, the G/CNT@MnO_2 composite as sulfur host is therefore proven to present effective polysulfide retention and redox conversion enhancement. On the one hand, ultrathin MnO_2 nanosheets can strongly interact with polysulfide species owing to the intrinsically polar property. As previously reported, $S_2O_3^{2-}$ generated from the reaction between long chain LiPSs and MnO_2 serves as an internal mediator to anchor the LiPSs, by forming insoluble polythionate and lower LiPSs.[14,17] On the other hand, the G/CNT@MnO_2 composites provide sufficient surface for charge transfer and lithium ion diffusion to implement the rapid electrochemical reaction. The excellent cycling stability can be attributed to the unique features of G/CNT@MnO_2@S nanocomposites. (i) The large surface area of G/CNT hybrids provide adequate space for MnO_2 nanosheets and sulfur particles which is beneficial to the uniform distribution of MnO_2 and high sulfur loading. (ii) The 3D architecture of G/CNT@MnO_2 composites provide large amount of charge transfer channels and Li^+ diffusion channels yielding a high rate performance and enhanced redox kinetics of LiPSs. (iii) Ultrathin MnO_2 nanosheets uniformly distributed on the surface of G/CNT hybrids enhance the chemical adsorption efficiency between MnO_2 and LiPSs, resulting in excellent cycling stability. (iv) The presence of nano-sized sulfur particles and their uniform distribution make best of sulfur and reinforce the cycling stability and rate performance of the fabricated Li–S batteries.

3. Conclusions

In summary, ultrathin MnO_2 decorated G/CNT nanocomposites used as S hosts were designed and synthesized through a facile redox deposition method. With the integrated structure design, G/CNT hybrids with superior conductivity and ultrathin MnO_2 nanosheets with uniform distribution enhanced the adsorption ability and redox reaction of LiPSs efficiently, thus exhibited stable cycling and high rate performance. As a result, a G/CNT@MnO_2@S nanocomposite with high sulfur loading of 81.8 wt% delivers a high initial specific capacity of 1015.1 mA h g^{-1} at a current density of 0.1C, with superior coulombic efficiency consistently near 100%. In particular, the G/CNT@MnO_2@S cathode exhibits high capacity retention of 84.1% and 77.9% at a rate of 0.1C and 1C, respectively. This facile method of fabricating G/CNT@MnO_2 nanocomposites constitutes a useful strategy for the design and synthesis of scalable, high-performance Li–S batteries.

Conflicts of interest

There are no conflicts to declare.

Acknowledgements

This work was supported by grants from the Program of Graphene Special Innovative Fund of AECC Beijing Institute of Aeronautical Materials.

Notes and references

1 M. P. Yu, J. S. Ma, H. Q. Song, A. J. Wang, F. Y. Tian, Y. S. Wang, H. Qiu and R. M. Wang, *Energy Environ. Sci.*, 2016, **9**, 1495–1503.

2 X. Fang and H. S. Peng, *Small*, 2015, **11**, 1488–1511.

3 M. A. Pope and I. A. Aksay, *Adv. Energy Mater.*, 2015, **5**, 1500124.

4 J. Yan, X. Liu and B. Li, *Adv. Sci.*, 2016, **3**, 1600101.

5 S. Y. Lang, Y. Shi, Y. G. Guo, D. Wang, R. Wen and L. J. Wan, *Angew. Chem.*, 2016, **55**, 15835–15839.

6 S. T. Zhang, M. B. Zheng, Z. X. Lin, N. W. Li, Y. J. Liu, B. Zhao, H. Pang, J. M. Cao, P. He and Y. Shi, *J. Mater. Chem. A*, 2014, **2**, 15889–15896.

7 W. Z. Bao, Z. Zhang, W. Chen, C. K. Zhou, Y. Q. Lai and J. Li, *Electrochim. Acta*, 2014, **127**, 342–348.

8 C. F. Zhang, B. W. Hao, C. Z. Yuan, Z. P. Guo and X. W. Lou, *Angew. Chem.*, 2012, **124**, 9730–9733.

9 J. C. Guo, Y. H. Xu and C. S. Wang, *Nano Lett.*, 2011, **11**, 4288–4294.

10 K. Mi, Y. Jiang, J. K. Feng, Y. T. Qian and S. L. Xiong, *Adv. Funct. Mater.*, 2016, **26**, 1571–1579.

11 J. Zhang, Z. M. Dong, X. L. Wang, X. Y. Zhao, J. P. Tu, Q. M. Su and G. H. Du, *J. Power Sources*, 2014, **270**, 1–8.

12 C. J. Hart, M. Cuisinier, X. Liang, D. Kundu, A. Garsuch and L. F. Nazar, *Chem. Commun.*, 2015, **51**, 2308–2311.

13 C. Li, Z. C. Xi, D. X. Guo, X. J. Chen and L. W. Yin, *Small*, 2018, **14**, 1701986.

14 X. Liang, C. Hart, Q. Pang, A. Garsuch, T. Weiss and L. F. Nazar, *Nat. Commun.*, 2015, **6**, 5682.

15 J. Guo, X. Zhang, X. Du and F. Zhang, *J. Mater. Chem. A*, 2017, **5**, 6447–6454.

16 Z. Chang, H. Dou, B. Ding, J. Wang, Y. Wang, X. Hao and D. R. MacFarlane, *J. Mater. Chem. A*, 2017, **5**, 250–257.

17 X. Liang, C. Y. Kwok, F. Lodi-Marzano, Q. Pang, M. Cuisinier, H. Huang, C. J. Hart, D. Houtarde, K. Kaup, H. Sommer, T. Brezesinski, J. Janek and L. F. Nazar, *Adv. Energy Mater.*, 2016, **6**, 1501636.

18 W. Li, J. Hicks-Garner, J. Wang, J. Liu, A. F. Gross, E. Sherman, J. Graetz, J. J. Vajo and P. Liu, *Chem. Mater.*, 2014, **26**, 3403–3410.

19 S. Rehman, T. Tang, Z. Ali, X. Huang and Y. Hou, *Small*, 2017, **13**, 1700087.

20 X. Liu, J. Q. Huang, Q. Zhang and L. Q. Mai, *Adv. Mater.*, 2017, **29**, 1601759.

21 X. Tao, J. Wang, C. Liu, H. Wang, H. Yao, G. Zheng, Z. W. Seh, Q. Cai, W. Li, G. Zhou, C. Zu and Y. Cui, *Nat. Commun.*, 2016, **7**, 11203.

22 D. Liu, C. Zhang, G. Zhou, W. Lv, G. Ling, L. Zhi and Q. H. Yang, *Adv. Sci.*, 2018, **5**, 1700270.

23 Z. Liu, B. Liu, P. Guo, X. Shang, M. Lv, D. Liu and D. He, *Electrochim. Acta*, 2018, **269**, 180–187.

24 Y. Li, D. Ye, W. Liu, B. Shi, R. Guo, H. Zhao, H. Pei, J. Xu and J. Xie, *ACS Appl. Mater. Interfaces*, 2016, **8**, 28566–28573.

25 X. Zhao, H. Wang, G. Zhai and G. Wang, *Chemistry*, 2017, **23**, 7037–7045.

26 X. C. Dong, B. Li, A. Wei, X. H. Cao, M. B. Chan-Park, H. Zhang, L.-J. Li, W. Huang and P. Chen, *Carbon*, 2011, **49**, 2944–2949.

27 J. Chen, J. H. Walther and P. Koumoutsakos, *Adv. Funct. Mater.*, 2015, **25**, 7539–7545.

28 M. Q. Zhao, X. F. Liu, Q. Zhang, G. L. Tian, J. Q. Huang, W. C. Zhu and F. Wei, *ACS Nano*, 2012, **6**, 10759–10769.

29 X. K. Huang, H. J. Yue, A. Attia and Y. Yang, *J. Electrochem. Soc.*, 2007, **154**, 26–33.

30 S.-B. Ma, K.-Y. Ahn, E.-S. Lee, K.-H. Oh and K.-B. Kim, *Carbon*, 2007, **45**, 375–382.

31 X. B. Jin, W. Z. Zhou, S. W. Zhang and G. Z. Chen, *Small*, 2007, **3**, 1513–1517.

32 Y. F. Dong, S. H. Liu, Z. Y. Wang, Y. Liu, Z. B. Zhao and J. S. Qiu, *Nanoscale*, 2015, **7**, 7569–7573.

33 X. Chen, S. J. Yan, N. Wang, S. K. Peng, C. Wang, Q. H. Hong, X. Y. Zhang and S. L. Dai, *RSC Adv.*, 2017, **7**, 55734–55740.

34 S. Liu, Y. Zhu, J. Xie, Y. Huo, H. Y. Yang, T. Zhu, G. Cao, X. Zhao and S. Zhang, *Adv. Energy Mater.*, 2014, **4**, 1301960.

35 N. Yu, H. Yin, W. Zhang, Y. Liu, Z. Tang and M.-Q. Zhu, *Adv. Energy Mater.*, 2016, **6**, 1501458.

36 Y. Munaiah, B. G. Sundara Raj, T. Prem Kumar and P. Ragupathy, *J. Mater. Chem. A*, 2013, **1**, 4300–4306.

37 C. Julien, M. Massot, R. Baddour-Hadjeanc, S. Frangerd, S. Bachd and J. P. Pereira-Ramosd, *Solid State Ionics*, 2003, **159**, 345–356.

38 S. Yang, X. Song, P. Zhang and L. Gao, *ACS Appl. Mater. Interfaces*, 2013, **5**, 3317–3322.

39 J. Yan, Z. Fan, T. Wei, W. Qian, M. Zhang and F. Wei, *Carbon*, 2010, **48**, 3825–3833.

40 R. Xu, J. Lu and K. Amine, *Adv. Energy Mater.*, 2015, **5**, 1500408.

41 Z. Li, J. Zhang and X. W. Lou, *Angew. Chem.*, 2015, **54**, 12886–12890.

42 H. W. Chen, C. H. Wang, W. L. Dong, W. Lu, Z. L. Du and L. W. Chen, *Nano Lett.*, 2015, **15**, 798–802.

43 G. H. Yuan, H. F. Jin, Y. Z. Jin and L. Z. Wu, *J. Solid State Electrochem.*, 2017, **22**, 693–703.

44 L. B. Ni, Z. Wu, G. J. Zhao, C. Y. Sun, C. Q. Zhou, X. X. Gong and G. W. Diao, *Small*, 2017, **13**, 1603466.

45 J. Zhang, Y. Shi, Y. Ding, W. K. Zhang and G. H. Yu, *Nano Lett.*, 2016, **16**, 7276–7281.

46 K. Cao, H. Liu, Y. Li, Y. Wang and L. Jiao, *Energy Storage Materials*, 2017, **9**, 78–84.

47 M. Sun, X. Wang, J. Wang, H. Yang, L. Wang and T. Liu, *ACS Appl. Mater. Interfaces*, 2018, **10**, 35175–35183.

48 X. Liang and L. F. Nazar, *ACS Nano*, 2016, **10**, 4192–4198.

49 F. Y. Fan and Y.-M. Chiang, *J. Electrochem. Soc.*, 2017, **164**, A917–A922.

50 X. K. Huang, K. Y. Shi, J. Yang, G. Mao and J. H. Chen, *J. Power Sources*, 2017, **356**, 72–79.

51 M. Yan, Y. Zhang, Y. Li, Y. Q. Huo, Y. Yu, C. Wang, J. Jin, L. H. Chen, T. Hasan, B. J. Wang and B. L. Su, *J. Mater. Chem. A*, 2016, **4**, 9403–9412.

52 J. Shen, J. Liu, Z. Liu, R. Hu, J. Liu and M. Zhu, *Chemistry*, 2018, **24**, 4573–4582.

53 L. B. Ni, G. J. Zhao, G. Yang, G. S. Niu, M. Chen and G. W. Diao, *ACS Appl. Mater. Interfaces*, 2017, **9**, 34793–34803.

54 L. B. Ni, G. J. Zhao, Y. T. Wu, Z. Wu, W. Wang, Y. Y. Liao, G. Yang and G. W. Diao, *Chem. - Asian J.*, 2017, **12**, 3128–3134.

55 C. Barchasz, F. Molton, C. Duboc, J. C. Leprêtre, S. Patoux and F. Alloin, *Anal. Chem.*, 2012, **84**, 3983–3980.

56 M. Chen, Q. Lu, S. Jiang, C. Huang, X. Wang, B. Wu, K. Xiang and Y. Wu, *Chem. Eng. J.*, 2018, **335**, 831–842.